Perovskite/Black Phosphorus/MoS$_2$ Photogate Reversed Photodiodes with Ultrahigh Light On/Off Ratio and Fast Response

Liming Wang,[†] Xuming Zou,[*,†] Jun Lin,[†] Jiayang Jiang,[†] Yuan Liu,[†] Xingqiang Liu,[†] Xu Zhao,[‡] Yu Fang Liu,[*,‡] Johnny C. Ho,[§] and Lei Liao[*,†]

[†]Key Laboratory for Micro/Nano Optoelectronic Devices of Ministry of Education & Hunan Provincial Key Laboratory of Low-Dimensional Structural Physics and Devices, School of Physics and Electronics, Hunan University, Changsha 410082, China

[‡]College of Physics and Material Science, Henan Normal University, Xinxiang 453007, China

[§]Department of Physics and Materials Science, City University of Hong Kong, Tat Chee Avenue, Kowloon, Hong Kong SAR 999077, China

Ⓢ *Supporting Information*

ABSTRACT: As compared with epitaxial semiconductor devices, two-dimensional (2D) heterostructures offer alternative facile platforms for many optoelectronic devices. Among them, photovoltaic based photodetectors can give fast response, while the photogate devices can lead to high responsivity. Here, we report a 2D photogate photodiode, which combines the benefits of 2D black phosphorus/MoS$_2$ photodiodes with the emerging potential of perovskite, to achieve both fast response and high responsivity. This device architecture is constructed based on the fast photovoltaic operation together with the high-gain photogating effect. Under reverse bias condition, the device exhibits high responsivity (11 A/W), impressive detectivity (1.3×10^{12} Jones), fast response (150/240 μs), and low dark current (3×10^{-11} A). All these results are already much better in nearly all aspects of performance than the previously reported 2D photodiodes operating in reverse bias, achieving the optimal balance between all figure-of-merits. Importantly, with a zero bias, the device can also yield high detectivity (3×10^{11} Jones), ultrahigh light on/off ratio (3×10^7), and extremely high external quantum efficiency (80%). This device architecture thus has a promise for high-efficiency photodetection and photovoltaic energy conversion.

KEYWORDS: photogate, photodiode, black phosphorus, MoS$_2$, perovskite, fast response
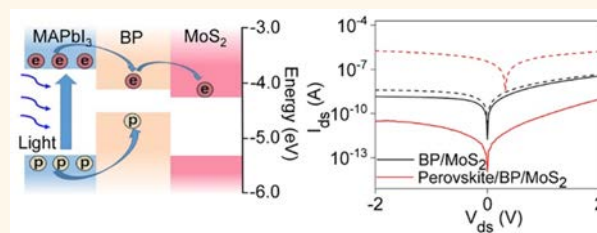
The ability of efficient sensing of optical radiation can enable many optoelectronic applications,such as industrial and environmental monitoring,[1] free-space communication,[2] remote-control scanning,[3] medical imaging,[4] *etc*. Regardless, all these utilizations require photodetectors with fast response, high detectivity ($D*$), low power consumption, and broad spectrum coverage as well as simple two-terminal operation. Early efforts have been focused on using epitaxial semiconductors (*e.g.*, group IV and III−V compounds) as the active device materials, but the required epitaxial synthesis methods make the device fabrication process extremely complicated. In contrast, due to the advent of nanotechnology, two-dimensional (2D) crystals based on atomically layered semiconductors, including graphene,[5,6] transitional metal dichalcogenides (TMDs),[7−9] and black phosphorus (BP),[10,11] can offer a facile platform for the effective photodetection because of their 2D nature, high carrier mobility, layer number dependent band structure, and more importantly their easy fabrication. In particular, these 2D

materials have no interlayer dangling bonds such that they can be configured in any arbitrary stacking sequences (*i.e.*, van der Waals (vdW) homo- or heterostructures) without the restriction of lattice registration, making them superior candidates for various optoelectronic applications.

Until now, the dominant operating mechanisms of these 2D based photodetectors are usually due to the photovoltaic and photogating effects. For example, photodiodes based on various p−n junctions are the most widely utilized photovoltaic devices, which are purposely designed to operate under reverse or zero bias condition. These junctions would contribute a controllable barrier for the efficient charge carrier transport during photodetection that gives the fast speed, large signal-to-noise ratio (SNR), and simple two-terminal operation.
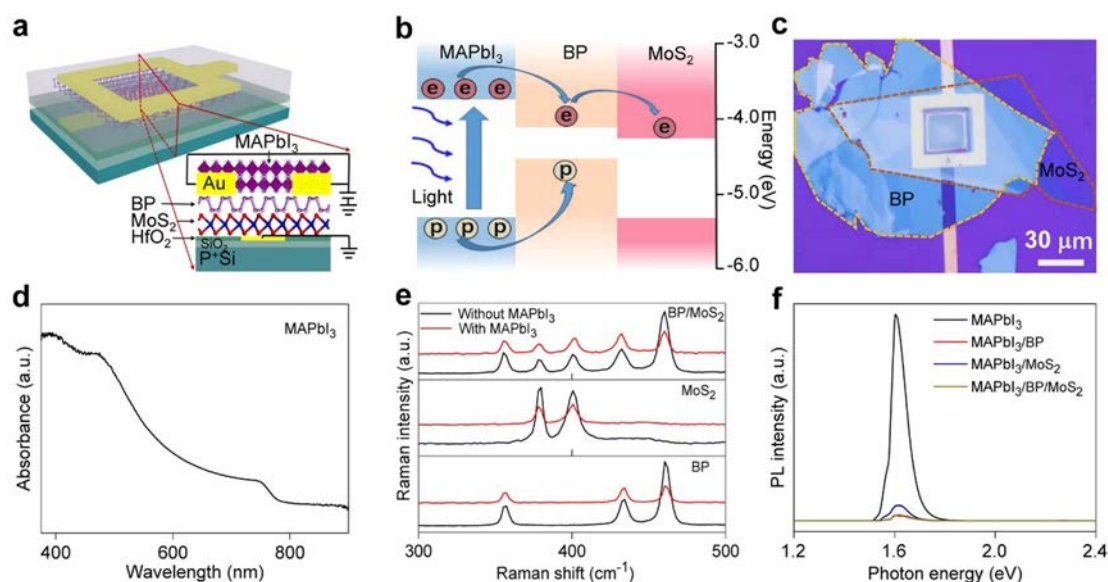
Figure 1. Design and characterization of the perovskite/BP/MoS$_2$ photodiode. (a) Schematic illustration of the proposed device. (b) Band diagram of the photogate photodiode and photocarriers transfer under laser illumination. (c) Optical image of a representative vertically stacked BP/MoS$_2$ photodiode. (d) Absorption spectra for the perovskite sample. (e) Raman spectra of the pristine and various hybrid structures measured under 532 nm laser excitation. (f) PL spectra measured for the MAPbI$_3$ perovskite film and the various hybrid structures.

However, these photodiodes do not provide the high photogain (G). Especially, for most 2D vdW heterostructure based photodiodes, the conduction band offset is typically smaller than interlayer exciton binding energy, resulting in an insufficient driving force for the photogenerated exciton dissociation. Combining with the relatively weak optical absorption of ultrathin 2D heterojunctions, the responsivity of these 2D photodiodes is hence limited to a range of 0.1 to 1 A/W under reverse or zero bias voltage.[12−18] In this case, to enhance their photoresponsivity, most of the 2D photodiodes as reported in the literature are operated under forward bias, which behave similar to a photoconductor, functioning with the photogating effect instead of the initially designed photovoltaic mechanism. This photogating effect is generally referred to the trap-assisted photoconductivity, where the photogenerated carriers would recirculate multiple times within the device channel filled with trap charges before recombination happens. In other words, these trapped charges can significantly prolong the recombination lifetime ($\tau_{lifetime}$) of photocarriers, leading to a high photogain according to the relationship of $G = \tau_{lifetime}/\tau_{transit}$. Here, $\tau_{transit}$ denotes the transit time. Inevitably, these long carrier lifetimes would yield the relatively slow response speed (in the scale of seconds to minutes)[19−23] since the trapping time cannot be controllably manipulated. In addition, the desired short transit time requires a high-conductivity device channel, which would at the same time give a large dark current. In view of all these problems, it is important to develop a more effective device architecture that would not curtailed by the above-mentioned operating mechanisms with photodetectors being either fast but insensitive, or sensitive but slow.

In this Letter, we present a facile and rational design of a fast and sensitive 2D photogate photodiode operating under reverse or zero bias condition. The device architecture is simply based on a vertically stacked BP/MoS$_2$ photodiode modified with a perovskite layer on the top. Specifically, the 2D photodiode is employed as the fast and convenient detecting platform, while the upper perovskite layer is used as a strong light absorption medium to enhance the responsivity. Upon 457 nm laser exposure, the perovskite modified BP/MoS$_2$ heterostructure can be operated as a reverse-biased photodiode with a maximum responsivity of 11 A/W. This value is about two orders of magnitude larger than those of other previously reported BP/MoS$_2$ photodiodes.[12,18] Also, the corresponding $D*$ value can be as high as 1.3×10^{12} Jones. Because of the built-in electric field existing at the BP/MoS$_2$ junction, the photocarrier separation and collection can as well be very efficient with the rise/decay time as low as 150/240 μs, respectively. It is worth mentioning that when this device is employed as a self-driven photodetector under zero bias, it exhibits a broadband photodetection ranging from all the way from visible light to near-infrared regimes with a high detectivity of 3×10^{11} Jones and an ultrahigh light on/off current ratio of 3×10^7. Furthermore, these 2D photogate photodiodes can also achieve an impressive photovoltaic power conversion, which exhibits a maximum external quantum efficiency around 80%, evidently demonstrating their promising potency for both high-performance photodetection and highly efficient light energy harvesting.

RESULTS AND DISCUSSION

Specifically, Figure 1a presents the schematic diagram of a 2D photogate photodiode proposed in this work. To achieve the broadband photodetector with fast response and good sensitivity, three criteria are necessary, which include the use of (i) a cost-effective photon absorption layer for the strong and broad-spectrum light harvesting; (ii) a type I heterointerface between the light absorption layer and adjacent 2D material to introduce sufficient photocarriers into the 2D p−n junction region; and (iii) a type II vdW heterointerface between the two 2D materials to enable effective photocarriers separation at the interface. In this regard, we come up with a device structure as shown in Figure 1a to satisfy all of these requirements. For details, few-layer MoS$_2$ and BP crystals are
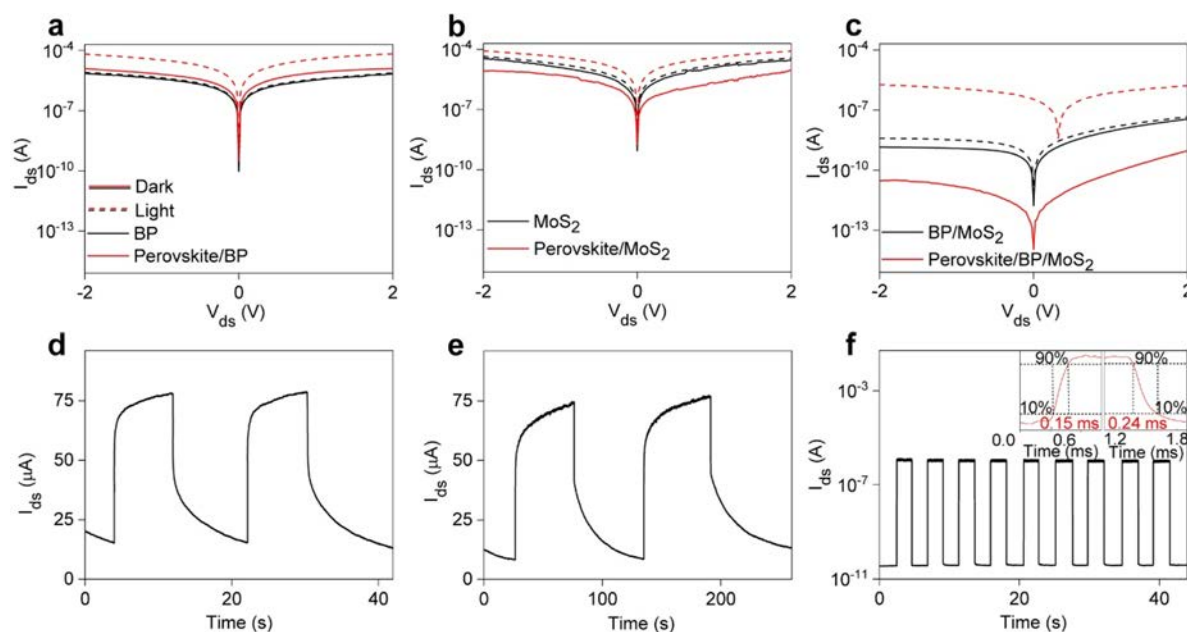
Figure 2. Photoresponse of the 2D photodetectors before and after the perovskite decoration. The $I_{ds}-V_{ds}$ characteristics of devices measured under dark and light conditions based on (a) BP and perovskite/BP, (b) MoS_2 and perovskite/MoS_2, and (c) BP/MoS_2 and perovskite/BP/MoS_2 structures, respectively. Dynamic response of the (d) perovskite/BP and (e) perovskite/MoS_2 photogate devices. (f) Dynamic response of the perovskite/BP/MoS_2 photogate diode. The inset shows the τ_{rise} (τ_{decay}) value of the device recorded by an oscilloscope.

employed to form the p−n photodiode due to their suitable band structure and superior carrier mobility.[18,23,24] Since the light absorption properties are anticipated to dictate the device performance as well as push forward the further enhancement on this particular device design, the research to achieve an effective light absorption layer here becomes very crucial. Although the organolead triiodide perovskite methylammonium lead iodide ($MAPbI_3$) has been widely explored as the light harvesting layer in many previous works due to its extraordinary optoelectronic properties for excellent photon-to-electron conversion,[21,23,25,26] its morphological development can be further improved with an assist from chlorine and thus yields a longer photocarrier diffusion length (~1 μm).[27] As a result, we focus on the $MAPbI_3$ perovskite with the use of chlorine precursors in this study. Figure 1b demonstrates the electronic band structure of our device, where the type I and type II heterojunctions are formed at the perovskite/BP and BP/MoS_2 interfaces, respectively. For perovskite materials, since the exciton binding energy is relatively small, this contributes to the excellent device performance of the detector. Explicitly, under illumination, when the photocarriers are spontaneously generated in the perovskite film, they would diffuse into the BP layer followed by photocarrier separation and collection due to the existence of built-in electric field at the BP/MoS_2 junction. This way, the detector photocurrent is simply determined by light harvesting in the upper perovskite layer and photocarrier separation at the BP/MoS_2 interface.

At the same time, the fabrication process of the vertically stacked photogate BP/MoS_2 diode is relatively straightforward and schematically illustrated in Supporting Information Figure S1, while Figure 1c exhibits the optical image of a representative fabricated device. Also, as displayed in Supporting Information Figure S2, film morphology of the as-prepared perovskite on silicon is characterized by scanning electron microscopy (SEM). It is clear that the film exhibits a compact polycrystalline texture with a conformal surface coverage. To further enhance the performance of these photogate devices, the perovskite film thickness is optimized to be ~200 nm for the most efficient light harvesting[22] (Figure S2 inset). X-ray diffraction (XRD) measurement is as well performed to investigate the crystallization characteristics of the obtained perovskite films. As presented in the spectrum in Supporting Information Figure S3, there are strong diffraction peaks located at 14.09°, 28.43°, 43.23°, and 58.90°, which are indexed as (110), (220), (330), and (440) $MAPbI_3$ planes, respectively, confirming the tetragonal structure there. Meanwhile, there are not any PbI_2 or $PbCl_2$ diffraction peaks observed in the spectrum, suggesting that the reaction of between $PbCl_2$ and methylammonium iodide is complete and a pure $MAPbI_3$ phase is formed. Moreover, Figure 1d exhibits the absorption spectrum of the as-fabricated perovskite film, in which strong and broadband light absorption in the UV−vis range is observed, revealing the excellent light absorbing characteristics of the $MAPbI_3$ layer.

In addition, Raman scattering measurements are also performed before and after perovskite decoration (Figure 1e). The observed Raman spectra from single BP or MoS_2 are consistent with the previous reports.[12] Importantly, the observed peaks of both BP and MoS_2 at the overlapping region have neglectable shift, indicating the good interface quality between BP and MoS_2 in the heterojunction. These features are further retained even after the perovskite layer capping, pointing toward that the perovskite film deposition via one-step method does not induce any structural damage to the BP and MoS_2 flakes as well as their heterointerface quality. The photoluminescence (PL) spectra of all different samples are as well measured (Figure 1f). It is anticipated the pristine perovskite film exhibiting a strong PL peak at 775 nm for its bandgap transition of $MAPbI_3$, while significant PL quenching effects are is observed for perovskite/BP, perovskite/MoS_2,
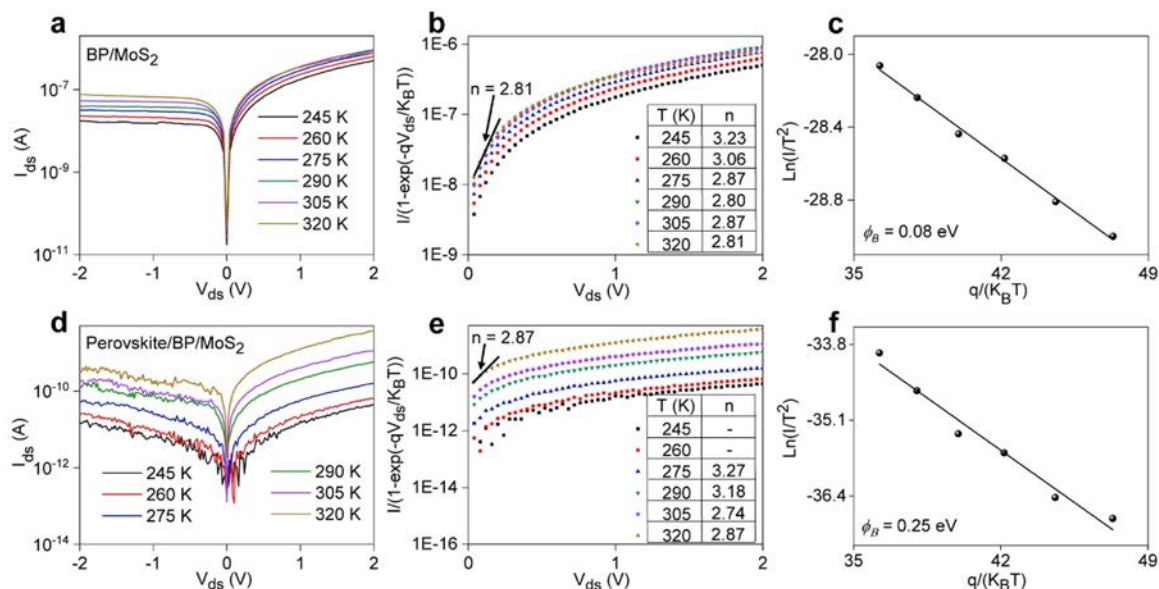
Figure 3. Temperature-related electrical measurements of a vertically stacked BP/MoS_2 photodiode before and after the perovskite decoration. (a) $I_{ds}-V_{ds}$ characteristics of the pristine BP/MoS_2 vertical heterojunction measured at different temperatures. (b) Ideality factor calculated with the slope of semilogarithmic graph derived from the pristine BP/MoS_2 heterojunction. (c) Semilog plot of I_{TE}/T^2 versus q/k_BT to extract the potential barrier height at the BP/MoS_2 junction before the perovskite deposition. (d) $I_{ds}-V_{ds}$ characteristics of the perovskite/BP/MoS_2 heterojunction measured at different temperatures. (e) Ideality factor calculated with the slope of semilogarithmic graph derived from the perovskite/BP/MoS_2 heterojunction. (f) Semilog plot of I_{TE}/T^2 versus q/k_BT to extract the potential barrier height at the BP/MoS_2 junction after the perovskite deposition.

and perovskite/BP/MoS_2 heterostructures due to the efficient exciton dissociation and interlayer charge transfer.

Apart from the confirmation of excellent light absorption and photocarrier separation, the photogating effect of these heterointegrated perovskite/BP and perovskite/MoS_2 hybrid photodetectors is thoroughly evaluated. As given in Supporting Information Figure S4, both pristine BP and MoS_2 devices exhibit linear and symmetric current−voltage ($I_{ds}-V_{ds}$) curves, which designate good ohmic contact between 2D semiconductors and metal electrodes. After deposition of perovskite layer onto BP device, the dark current is about an order of magnitude higher than the one of the single BP (Figure 2a). In this perovskite/BP heterostructured photodetector, the device current is attributed to the carrier transport in both BP and perovskite layers; however, the carrier mobility associated with the perovskite layer is only in the order of 1×10^{-4} cm^2/V s (ref 22), being much lower than the BP layer of 417 cm^2/V s (Supporting Information Figure S5). In this case, the carrier transport in perovskite layer is insignificant; therefore, the dark current increase here can be attributed to the enhanced carrier transport in the BP channel with the perovskite capping layer. We then compare the transfer characteristic of the BP transistor before and after the perovskite deposition (Supporting Information Figure S5). The pristine BP field-effect transistor (FET) exhibits an excellent gate modulated current with a high on/off ratio of around 10^4. After capping with the perovskite layer, the FET characteristic is maintained but with a more positive threshold voltage, suggesting the existence of a p-type doping effect. This is probably due to the hole transfer from perovskite layer into BP, which subsequently lowers the Fermi level of BP and induces the barrier reduction of hole injection at the Au/BP interface. In the case of the perovskite/MoS_2 bilayer device, similar p-type doping is also observed. Likewise, the Fermi level of MoS_2 is lowered, which leads to the barrier increase of electron injection at the Au/MoS_2

interface. Therefore, the dark current is significantly reduced here (Figure 2b). In other words, under illuminated conditions (*e.g.*, light power density (P_{light}) = 119 mW/cm^2 and wavelength (λ) = 457 nm), electron−hole pairs would be first generated in the top perovskite layer, in which their concentration is highly depended on the film morphology.[28] Subsequently, the electron−hole pairs would split due to the ambipolar transport characteristic of perovskite film and then diffuse into the BP or MoS_2 region. Also, there is an obvious threshold voltage (V_{th}) shift of the device once upon illumination. This V_{th} shift reflects the photogating effect playing a dominant role in the photocurrent generation. On the other hand, to assess the response of the device to the laser power, the photo responsivity (R) is calculated by the following analytical equation:

$$R = \frac{I_{light} - I_{dark}}{P_{light}S} = \frac{I_{ph}}{P_{light}S} \tag{1}$$

Here, I_{dark} and I_{light} are the output currents under dark and illumination, respectively, I_{ph} is the photocurrent, and S is the illumination area. As a result, in comparison with the pristine device, the responsivity of both perovskite/BP and perovskite/MoS_2 photodetectors are increased by about 79-times (11 to 872 A/W) and 11-times (120 to 1342 A/W), correspondingly (Supporting Information Figure S6). This greatly enhanced responsivity probably arises from the trap states that exist either in the 2D materials or at the heterointerfaces. In general, these trap states are mainly contributed by two sources, including the impurities or vacancies existed in the 2D materials as well as the surface contamination associated with fabrication processes. In any case, under illumination, the photocarriers would fill most of the trap states and remain there. Because of the long trapping time, the lifetime of the photocarriers (*i.e.*, of the opposite charge type of the traps) is

prolonged in these 2D channels, which eventually leads to the substantially enhanced photogain. However, the issue of slow response associate with the photogate device also emerges. The temporal photoresponse characteristics of both perovskite/BP and perovskite/MoS$_2$ devices are exhibited in Figure 2d and e, respectively. The rise time (τ_{rise}) and the decay time (τ_{decay}) are measured to be 1.3 and 5.7 s for the perovskite/BP device, and 16 and 30 s for the perovskite/MoS$_2$ device, correspondingly. The rise (decay) time here represents the period of the current to increase (decrease) from 10% to 90% (from 90% to 10%) of the maximum value. These problematically slows response time arising from the persistent trapped charges severely restricts the practical applications of photogate devices.

Next, the hybrid 2D photogate photodiode is also electrically characterized under the same condition. Figure 2c shows the I–V curve of a typical p–n diode based on the fabricated BP/MoS$_2$ heterostructure, which exhibits an obvious rectifying behavior with a rectification ratio of 20. After capping with the perovskite layer, the device dark current is lowered by approximately two orders of magnitude than that of the pristine BP/MoS$_2$ device. This result well supports the p-doping phenomenon on the BP channel as described above. Notably, since the BP and MoS$_2$ flakes form the type-II heterostructure (will be discussed in details in Figure 3), some electrons are transferred from MoS$_2$ into BP to achieve the electron potential balance, resulting in the built-in potential formation across the BP/MoS$_2$ interface. As a forward bias is applied, this built-in potential would decrease and the conducting electrons can be more easily drifted from MoS$_2$ to BP, yielding the on-state. In comparison, as a reverse bias is applied, the built-in potential would increase and fewer electrons can flow across the barrier, leading to the off-state of the device. Simultaneously, because of the p-type doping in BP, its Fermi level is lowered, in which the energy band upshifts. Consequently, the energy band of MoS$_2$ is shifted down, thereby increasing the effective barrier height at the BP/MoS$_2$ junction. This way, the carrier injection probability is expected to be reduced under both forward and reverse bias. In comparison, the inverted MoS$_2$/BP photodiode exhibits an increased dark current after the perovskite deposition (Supporting Information Figure S7). This can be understood by that the p-type doping of MoS$_2$ reduces the barrier height at the BP/MoS$_2$ junctions, which will give the higher dark current there. As a result, the perovskite/BP/MoS$_2$ device architecture is more suitable for the weak-light detection because of its advantages of the lower dark current and higher p–n junction electric field for the efficient carrier separation.

Interestingly, under a reverse bias of V_{ds} = −2 V, the pristine BP/MoS$_2$ photodiode exhibits a slightly higher light-to-dark current ratio (I_{light}/I_{dark}) than the one extracted at V_{ds} = +2 V (2.8 to 1.3), but a lower responsivity (8.1 to 31.5 A/W). The virtue of the photogate p–n diode (i.e., perovskite/BP/MoS$_2$) can be immediately recognized when comparing the I_{light}/I_{dark} values here. For example, under a bias of −2 V, the calculated I_{light}/I_{dark} value of the photogate diode is ∼60 000, which is ∼20 000-times higher than the pristine BP/MoS$_2$ device. Also, the I_{dark} value of the photogate diode is as low as 30 pA. Meanwhile, the responsivity is increased by about 740-times (1.7 A/W to 2.3 mA/W) after the perovskite capping. This value is even higher than the one operated with the forward bias condition of the pristine BP/MoS$_2$ device (R = 1.4 A/W at V_{ds} = 2 V). In conventional p–n photodiodes, the reverse

photocurrent is highly dependent on the number of photo-excited minority carriers in depletion region, while the forward current is dedicated by the velocity of charge carrier in the device channel. Because of the weak optical absorption and strong binding energy of interlayer excitons, the photoinduced free-carriers are quite limited in the 2D heterojunction. Therefore, the value of I_{light} is expected to be low in the BP/MoS$_2$ photodiode and remained the same under the constant incident laser power, where the value also does not vary with the increasing reverse bias. In comparison, there are abundant photocarriers generated in the top perovskite absorption layer in the 2D photogate photodiode, in which these carriers are subsequently transferred into the p–n junction region. Because of the photogating effect, the photoresponse is substantially enhanced here. Importantly, the intrinsic issue of slow response of p–n diodes is also resolved with this enhanced device architecture. Figure 2f displays the on–off switching characteristic of the perovskite/BP/MoS$_2$ device, exhibiting the reliable and fast on–off switching repetition in multiple-cycle tests. In Figure 2f inset, the high-resolution temporal photoresponse is measured by oscilloscope, where the τ_{rise} and τ_{decay} values are recorded to be 150 and 240 μs, respectively. In this photogate p–n photodiode, the photocarrier separation and recombination are controlled by the enhanced p–n junction as described above, in which this process is known to be much faster than the one of trap-assisted photocarrier separation and recombination. As a result, it is understood that the response speed of the perovskite/BP/MoS$_2$ device is much faster than the conventional photogate devices.

In addition, it is evident that the perovskite/BP/MoS$_2$ device also exhibits an impressive photovoltaic behavior, which is in a distinct contrast to the pristine BP/MoS$_2$ device without any perovskite capping. To understand the photovoltaic phenomenon, temperature (T) related electrical measurements are thoroughly carried out to further our insights into the interface characteristics of the vertically stacked heterostructure device. Specifically, the barrier height at the BP/MoS$_2$ junction can be extracted from these measurements. The heterojunction current before and after perovskite capping can be understood with the thermionic emission theory:[29,30]

$$I_{ds} = I_{TE} \exp\left(\frac{qV_{ds}}{nk_BT}\right)\left[1 - \exp\left(-\frac{qV_{ds}}{k_BT}\right)\right] \quad (2)$$

$$I_{TE} \propto T^2\left[\exp\left(-\frac{q\phi_B}{k_BT}\right)\right] \quad (3)$$

where I_{TE} denotes the saturation current, k_B denotes the Boltzmann constant, n denotes the ideality factor, and q denotes the electron charge. This way, we can extract the n value and the Schottky barrier height (ϕ_B) at the BP/MoS$_2$ junction. On the basis of the semilog plots of $I_{ds}/[1 - \exp(-qV_{ds}/k_BT)]$ versus V_{ds} (Figure 3b,e), the slopes of linear regions give the ideality factor around 3 for all temperature values. In terms of n value, the results are much better than heterojunction p–n diodes configured with bulk materials ($n \gg 2$)[31] and TMDs ($n \approx 6.5$),[32] but worse than TMDs homojunctions fabricated by chemical doping ($n \approx 1.6$)[33] or gate modulation ($n \approx 1.9$).[34] The n value of any junction provides the level to which defects influence carrier transport. n
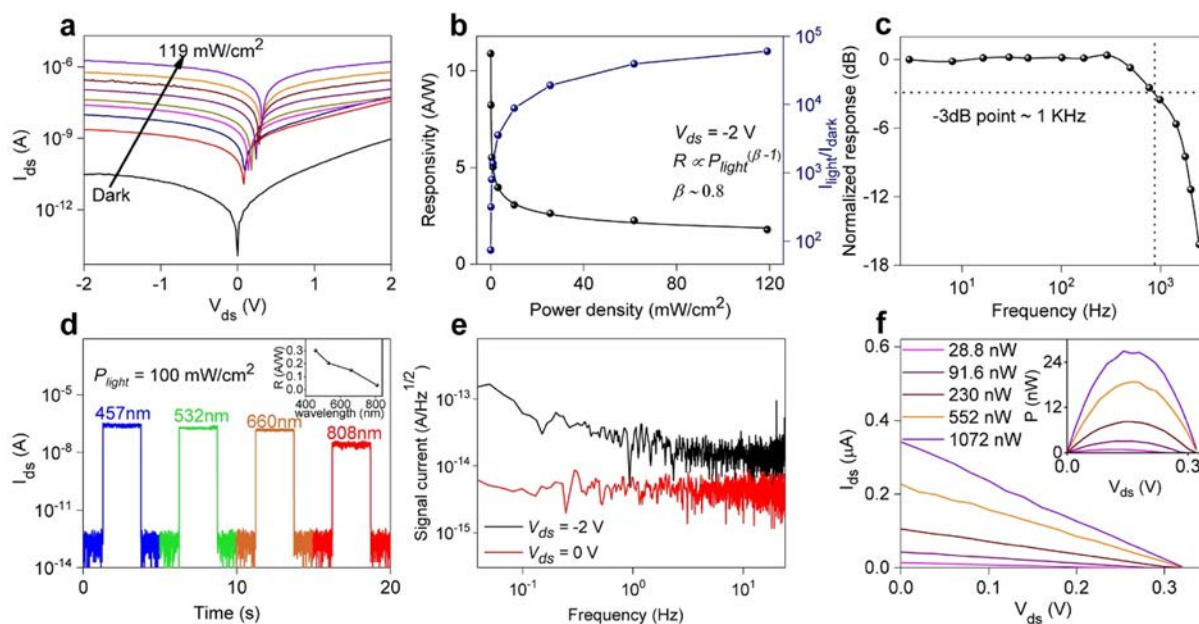
Figure 4. Optoelectronic characteristics of the perovskite/BP/MoS$_2$ photogate photodiode operated under reverse and zero bias modes. (a) I_{ds}−V_{ds} curves of the device at a reverse bias of −2 V under 457 nm laser illumination. (b) Extracted R and I_{light}/I_{dark} values on the basis of measured incident power at a reverse bias of −2 V. (c) Normalized response loss of the device versus the light modulation frequency at a reverse bias of −2 V. (d) Response of the device operated under zero bias mode with different wavelengths of 457, 532, 660, and 808 nm. The inset shows the corresponding responsivity. (e) Noise analysis of the perovskite/BP/MoS$_2$ photodiode extracted from the Fourier transform of the dark current. (f) I_{ds}−V_{ds} curves under different power intensity. The I_{sc} and V_{oc} can be obtained from the intercepts of the curves on I_{ds} and V_{ds} axes, respectively. The inset shows the power generated by the device as a function of V_{ds} under different laser power.

= 1 implies the ideal diode behavior with entirely thermionic carrier transport across p−n junction. Here, the extracted n values indicate the existence of interface charge traps in our p−n diodes. More importantly, using the saturation current for different temperatures, a semilog plot of I_{TE}/T^2 versus q/k_BT (Figure 3c) would give a SBH value of ∼0.08 eV for the standard BP/MoS$_2$ diode, a substantially larger value of ∼0.25 eV with the perovskite capping (Figure 3f). All these indicate that the BP/MoS$_2$ forms type II p−n junction here, which is favorable for achieving this improved photogate p−n photodiode. It can also be inferred that the enhanced barrier height at the BP/MoS$_2$ junction is responsible for the evident photovoltaic behavior after perovskite deposition.

Furthermore, the optoelectronic properties of the photogate p−n photodiode are examined in detail. Figure 4a exhibits the output curves of the device upon 457 nm laser illumination. Under reverse bias condition (V_{ds} = −2 V), the responsivity and I_{light}/I_{dark} values are observed to be strongly influenced by the laser power (Figure 4b). For instance, the responsivity decreased as the P_{light} value increased, which is probably due to the enhanced photocarriers recombination with the increasing light intensity. The highest responsivity at P_{light} = 0.02 mW/cm^2 is 11 A/W. This value is approximately two orders of magnitude higher than the previously reported reverse-biased BP/MoS$_2$ photodiode, and much higher than that of typical 2D material reverse-biased photodiodes and the Si based photodiodes (∼0.8 A/W).[35,36] Meanwhile, the I_{light}/I_{dark} value increases with the light intensity. At P_{light}= 119 mW/cm^2, the highest I_{light}/I_{dark} value is extracted to be ∼6 × 10^4. Additionally, photogain is a critical parameter to evaluate the detector performance, which determines the number of photocarriers induced per incident photon, while it can always be estimated with following equation:

$$G = \frac{I_{ph}/q}{P_{light}/h\nu} = R\frac{hc}{q\lambda}$$

(4)

where h is the Planck constant, c is the speed of light, and ν is the incident photon frequency, respectively. With the extracted maximum R value of 11 A/W, the photogain is determined to be 30. Thus, the photocarriers can circulate multiple times in the whole circuit before recombination, demonstrating a decent photogating effect associated with our perovskite/BP/MoS$_2$ devices. The temporal response bandwidth of the photodetector operating at reverse bias mode is also evaluated with the 3 dB bandwidth. The result represents a frequency limitation that the photocurrent induced by the optical signal is 0.707-times the maximum value. As shown in the measured frequency response in Figure 4c, the 3 dB point is located at ∼1 kHz using an illumination source of P_{light}= 119 mW/cm^2. Although this value is lower than the commercially available Si-based photodiode, these values still seem very attractive in view of the early stage of the device development here. Substantial improvement in the temporal response of photogate photodiodes can be further achieved by reducing the interface trap density with the oxygen-free fabrication process and enhancing the built-in electric field at the p−n junction by exploiting more suitable 2D materials.

Another important observation is that the photogate p−n photodiode can also be performed as a high-performance self-driven photodetector. In comparison with other photodetectors, this type of devices possesses the advantage in weak signal detection due to their greatly suppressed dark current with zero bias operation. Besides, the self-driven photodetectors also exhibit several other merits, including ease of operation, energy conservation, and suitable for working under extreme conditions. Here, the self-driven operation of

Table 1. Comparison of Different Important Device Parameters of Various 2D Heterostructure Photodetectors

materials	wavelength (nm)	R (A/W)	I_{dark} (nA)	I_{light}/I_{dark}	D^* (Jones)	T_{rise}/T_{decay} (ms)	gain	ref
perovskite/BP/MoS$_2$	457	11	~0.03	~6×10^4	1.3×10^{12}	0.15/0.24	30	this work
BP/Monolayer MoS$_2$	633	0.42	~2	~19			0.82	12
BP/MoS$_2$	532	0.17					0.39	18
WSe$_2$/MoS$_2$	532	0.17	~0.03	~3×10^4		<0.1/< 0.1	0.39	14
MoS$_2$/WS$_2$	633	1.42	~100	~9	~1.7×10^{10}		2.78	15
WSe$_2$/WS$_2$	633					<20		16
MoTe$_2$/MoS$_2$	470	0.322	~0.01	~800		~25	0.85	17
GaTe/MoS$_2$	633	1.365				<10	2.7	13

the perovskite/BP/MoS$_2$ device is evidently witnessed. As presented in the photocurrent switching performance at different incident wavelength (P_{light} = 100 mW/cm^2) in Figure 4d, the photocurrent decreases with the increasing λ value. This is probably due to the relatively poor light absorption capacity and reduced photon energy at long wavelength. However, obvious photoresponses are also observed without applying any bias and can be modulated effectively by the incident light power. At a fixed P_{light} value of 100 mW/cm^2, the responsivity is found to be 0.3, 0.2, 0.15, and 0.03 A/W at the wavelength of 457, 532, 660, and 808 nm, respectively. In fact, the spectral responsivity of the 2D photogate photodiode relies heavily on the optical absorbance of perovskite layer. This particular device structure is expected to be capable to detect the incident light with an even longer wavelength by using the top absorption layer with a smaller bandgap.

In addition to the above performance assessment, specific detectivity is another key parameter to evaluate the device capability of detecting weak light irradiation. The detectivity is typically estimated by the following relationship:[5,37−39]

$$D^* = \frac{(SB)^{1/2}}{NEP} \tag{5}$$

$$NEP = \frac{\overline{i_n^2}^{1/2}}{R} \tag{6}$$

Here, NEP denotes the noise equivalent power, B denotes the bandwidth, and $\overline{i_n^2}^{1/2}$ denotes the root−mean−square value of the noise current. In detail, Figure 4e shows the noise level per unit bandwidth (1 Hz) of the device. Using the R values of 11 A/W at $V_{ds} = -2$ V and 0.3 A/W at $V_{ds}= 0$ V, the corresponding D^* values can be calculated as 1.3×10^{12} and 3×10^{11} Jones, respectively. Here, the extracted values under reverse or zero bias condition are superior to those of the traditional silicon photodetectors.

Apart from responsivity and detectivity, the signal-to-noise ratio and linear dynamic range (LDR) are also recognized as two important parameters to evaluate photodetector performance. Specifically, the SNR value represents the ratio of external signal to device background noise. Apparently, a higher SNR value would give the less obtrusive background noise. On the other hand, LDR gives the detecting region of incident light power where the device can distinguish the incident light signal and is usually described with decibels (dB).[40] Providing the measured output currents under dark and illumination, the SNR and LDR values can be estimated with the following equation:[41]

$$SNR = \frac{I_{light} - I_{dark}}{I_{dark}} \tag{7}$$

$$LDR = 20 \log \frac{J_{light}}{J_{dark}} \tag{8}$$

where J_{dark} is the dark current density, and J_{light} is the current density measured at P_{light} = 1 mW/cm^2, respectively.[40] Accordingly, the calculated SNR and LDR values of the photogate diode at 457 nm wavelength are presented in Supporting Information Figure S8. The device displays an ultrahigh SNR value of 3×10^7 under zero bias, which arises from the high photoresponsivity and low dark current. It is also worth pointing out that the corresponding I_{light}/I_{dark} value is as high as 3×10^7, which is much higher than that of the previously reported 2D materials photodetectors even assisted by ferroelectric field and gate modulation.[42,43] Moreover, the LDR value is calculated to be 111 dB. This decent value is already comparable with those of Si-based photodetectors of 120 dB and much higher than that of InGaAs-based photodetectors of 66 dB.[44] Table 1 presents the important performance parameters of different 2D heterostructure photodetectors operated under reverse or zero bias condition. It is evident that the present device performs much better than those of previously reported 2D photodiodes, achieving the optimal balance between all key performance parameters.

Besides photodetection, this photogate p−n photodiode is also employed for the photovoltaic energy harvesting as shown in Figure 4f. Here, the open circuit voltage (V_{oc}) of the device is relatively low at the weak light intensity, probably due to the photocarriers recombination; correspondingly, as the incident light intensity increases, the amount of photocarriers increases simultaneously, inducing the rise of V_{oc} value. In this case, the device exhibits a maximum V_{oc} value of 0.32 V and a short circuit current (I_{sc}) of up to 0.34 μA under 457 nm illumination (119 mW/cm^2). With the information, the power generated in the photogate photodiode can be estimated accordingly (Figure 4f inset). Also, the external quantum efficiency (EQE) of the device at V_{ds} = 0 V can be evaluated by the following equation:

$$EQE = \frac{I_{sc}hc}{P_{light}e\lambda} \tag{9}$$

The corresponding EQE value is calculated to be ~80%, which is significantly higher than those reported previously 2D heterojunctions devices.[45,46] This impressive EQE value can be mainly attributed to the high light absorption of the top perovskite layer as well as the efficient diffusion of photocarriers in the BP/MoS$_2$ p−n diode. All these results clearly demonstrate the promising potency of utilizing this device structure for the highly effective photovoltaic energy conversion.

CONCLUSIONS

In summary, we propose and develop a hybrid 2D photogate photodiode based on perovskite and BP/MoS$_2$ photodiode. As compared with conventional detectors utilizing photovoltaic and photogating mechanisms, this hybrid device exhibits both high responsivity and fast response. At a reverse bias of −2 V, the responsivity of perovskite/BP/MoS$_2$ device can be greatly improved to 11 A/W, while the device response time can be optimized down to hundreds of microseconds, being few orders of magnitude faster than those obtained in high-gain photogate devices. The corresponding detectivity is as high as 1.3×10^{12} Jones. Also, due to the effective light absorption of perovskite and large electric field established in the BP/MoS$_2$ junction, this hybrid device is highly suitable for the self-driven broadband photodetection. Under 457 nm laser illumination and zero bias condition, the device shows a high detectivity of 3×10^{11} Jones and an ultrahigh I_{light}/I_{dark} value of 3×10^7. In addition, the hybrid device as well demonstrates the efficient photovoltaic power conversion with a peak EQE value of 80%. Evidently, this high-performance 2D photogate photodiode is advantageous for practical applications, whereas its integration capability of 2D heterostructures with strong optical absorption layers would provide great opportunities for the developing optoelectronic devices.

METHODS

Atomic Layer Deposition (ALD) Growth of HfO$_2$. ALD growth of HfO$_2$ was carried out employing tetrakis(dimethylamino)hafnium (TDMAH) and H$_2$O precursors at 95 °C. During the process, the H$_2$O source temperature was 25 °C, while the TDMAH source temperature was 90 °C. High purity Ar$_2$ was used as carrier gas. The TDMAH purge was applied with Ar$_2$ for 120 s, whereas the post H$_2$O purge was 100 s. The resulting growth rate was approximately 1.2 Å/ cycle.

Device Fabrication. Few-layer MoS$_2$ and BP and flakes were obtained with mechanically exfoliated method and then transferred onto the marked p$^+$-Si/SiO$_2$ substrates. Subsequently, poly(methyl methacrylate) (PMMA) was spin-coated onto the substrates, and then the electrode patterns were defined by E-beam lithography. After that, the Au electrodes were formed by metal evaporation and the lift-off process. At the end, the fabricated BP and MoS$_2$ transistors were heated at 200 °C for 1 h in a nitrogen-filled glovebox to minimize the contact resistance.

Similarly, the fabrication of vertically stacked BP/MoS$_2$ p−n photodiode was initiated by defining a bottom Au electrode onto a SiO$_2$/p$^+$-Si substrate. The electron beam lithography (EBL) process was performed to have the square pattern (30 × 30 μm^2) in the PMMA resist precoated onto the processed substrate. A 15 nm thick of HfO$_2$ layer is then deposited by ALD. After that, unwanted HfO$_2$ film located within the square pattern could be removed by a lift-off process using acetone. Few-layer MoS$_2$ flake was next transferred onto the Au bottom electrode employing the polydimethylsiloxane (PDMS) stamp. Consequently, the similar process was performance to transfer few-layer BP nanosheet onto the MoS$_2$/Au sample. At the end, the top Au electrode was patterned onto the BP avoiding the BP/MoS$_2$ overlapping region via standard lithography and lift-off processes.

For the preparation of the above-mentioned top perovskite layer, MAI and PbCl$_2$ (with a 3:1 molar ratio) were first dissolved into anhydrous N,N-dimethylformamide in a glovebox filled with nitrogen. The mixture was then stirred at 45 °C for 8 h to obtain the precursor solution. Subsequently, the obtained mixed halide perovskite solution was deposited onto the prepared device substrates via spin-coating at 4000 rpm for 1 min. At the end, the sample was annealed for 1 h at 100 °C to form a MAPbI$_3$ perovskite film (∼200 nm) on the BP/ MoS$_2$ device.

Material Characterization and Device Measurement. SEM (JEOL 6510) is employed to characterize the perovskite film morphologies. The absorption spectra were performed with the UV−vis spectrometer (Shimadzu UV-2550). XRD measurement was carried out at room temperature employing the X-ray Diffractometer (Rigaku SmartLab). PL was performed at room temperature employing a excitation laser of 532 nm. Electrical and optoelectrical measurements were carried out by employing a standard probe station and the Agilent B1500A Semiconductor Parameter Analyzer. The light sources were lasers with wavelengths of 457, 532, 660, and 808 nm, respectively.

ASSOCIATED CONTENT

⑤ Supporting Information

The Supporting Information is available free of charge on the ACS Publications website at DOI: 10.1021/acsnano.9b01713.

Fabrication procedure of vertically stacked BP/MoS$_2$ p−n diodes; SEM image and XRD spectrum of perovskite layer; I_{ds}−V_{ds} curves of BP, MoS$_2$, MoS$_2$/BP, and perovskite/MoS$_2$/BP devices; photoresponse of BP, MoS$_2$, and BP/MoS$_2$ devices before and after perovskite deposition (PDF)

AUTHOR INFORMATION

Corresponding Authors
*E-mail: liaolei@whu.edn.cn.
*E-mail: zouxuming@hnu.edu.cn.
*E-mail: yf-liu@htu.cn.

ORCID ⊙
Yuan Liu: 0000-0002-0024-9290
Johnny C. Ho: 0000-0003-3000-8794
Lei Liao: 0000-0003-1325-2410

Notes
The authors declare no competing financial interest.

REFERENCES

(1) Willer, U.; Saraji, M.; Khorsandi, A.; Geiser, P.; Schade, W. Near-and Mid-Infrared Laser Monitoring of Industrial Processes, Environment and Security Applications. *Opt. Lasers Eng.* **2006**, *44*, 699−710.

(2) Soref, R. Mid-Infrared Photonics in Silicon and Germanium. *Nat. Photonics* **2010**, *4*, 495−497.

(3) Yuang, R.-H.; Chyi, J.-I.; Lin, W.; Tu, Y.-K. High-Speed Ingaas Metal-Semiconductor-Metal Photodetectors with Improved Responsivity and Process Yield. *Opt. Quantum Electron.* **1996**, *28*, 1327−1334.

(4) Zecchina, A.; AreÁN, C. O. Diatomic Molecular Probes for Mid-IR Studies of Zeolites. *Chem. Soc. Rev.* **1996**, *25*, 187−197.

(5) Kim, C. O.; Kim, S.; Shin, D. H.; Kang, S. S.; Kim, J. M.; Jang, C. W.; Joo, S. S.; Lee, J. S.; Kim, J. H.; Choi, S.-H.; et al. High Photoresponsivity in An All-Graphene PN Vertical Junction Photodetector. *Nat. Commun.* **2014**, *5*, 3249.

(6) Xia, F.; Mueller, T.; Lin, Y.-M.; Valdes-Garcia, A.; Avouris, P. Ultrafast Graphene Photodetector. *Nat. Nanotechnol.* **2009**, *4*, 839−843.

(7) Lopez-Sanchez, O.; Lembke, D.; Kayci, M.; Radenovic, A.; Kis, A. Ultrasensitive Photodetectors Based on Monolayer MoS_2. *Nat. Nanotechnol.* **2013**, *8*, 497−501.

(8) Perea-Lopez, N.; Elias, A. L.; Berkdemir, A.; Castro-Beltran, A.; Gutierrez, H. R.; Feng, S.; Lv, R.; Hayashi, T.; Lopez-Urias, F.; Ghosh, S.; Muchharla, B.; Talapatra, S.; Terrones, H.; Terrones, M. Photosensor Device Based on Few-Layered WS_2 Films. *Adv. Funct. Mater.* **2013**, *23*, 5511−5517.

(9) Jin, Y.; Keum, D. H.; An, S.-J.; Kim, J.; Lee, H. S.; Hee, Y. A Van Der Waals Homojunction: Ideal P-N Diode Behavior in $MoSe_2$. *Adv. Mater.* **2015**, *27*, 5534−5540.

(10) Engel, M.; Steiner, M.; Avouris, P. Black Phosphorus Photodetector for Multispectral, High-Resolution Imaging. *Nano Lett.* **2014**, *14*, 6414−6417.

(11) Buscema, M.; Groenendijk, D. J.; Blanter, S. I.; Steele, G. A.; Van Der Zant, H. S. J.; Castellanos-Gomez, A. Fast and Broadband Photoresponse of Few-Layer Black Phosphorus Field-Effect Transistors. *Nano Lett.* **2014**, *14*, 3347−3352.

(12) Deng, Y.; Luo, Z.; Conrad, N. J.; Liu, H.; Gong, Y.; Najmaei, S.; Ajayan, P. M.; Lou, J.; Xu, X.; Ye, P. D. Black Phosphorus-Monolayer MoS_2 Van Der Waals Heterojunction P-N Diode. *ACS Nano* **2014**, *8*, 8292−8299.

(13) Yang, S.; Wang, C.; Ataca, C.; Li, Y.; Chen, H.; Cai, H.; Suslu, A.; Grossman, J. C.; Jiang, C.; Liu, Q.; Tongay, S. Self-Driven Photodetector and Ambipolar Transistor in Atomically Thin GaTe-MoS_2 P-N Vdw Heterostructure. *ACS Appl. Mater. Interfaces* **2016**, *8*, 2533−2539.

(14) Lee, H. S.; Ahn, J.; Shim, W.; Im, S.; Hwang, D. K. 2D WSe_2/MoS_2 Van Der Waals Heterojunction Photodiode for Visible-Near Infrared Broadband Detection. *Appl. Phys. Lett.* **2018**, *113*, 163102.

(15) Huo, N.; Kang, J.; Wei, Z.; Li, S.-S.; Li, J.; Wei, S.-H. Novel and Enhanced Optoelectronic Performances of Multilayer MoS_2-WS_2 Heterostructure Transistors. *Adv. Funct. Mater.* **2014**, *24*, 7025−7031.

(16) Huo, N.; Yang, J.; Huang, L.; Wei, Z.; Li, S.-S.; Wei, S.-H.; Li, J. Tunable Polarity Behavior and Self-Driven Photoswitching in P-WSe_2/N-WS_2 Heterojunctions. *Small* **2015**, *11*, 5430−5438.

(17) Pezeshki, A.; Shokouh, H.; Nazari, T.; Oh, K.; Im, S. Electric and Photovoltaic Behavior of A Few-Layer Alpha-$MoTe_2$/MoS_2 Dichalcogenide Heterojunction. *Adv. Mater.* **2016**, *28*, 3216−3222.

(18) Hong, T.; Chamlagain, B.; Wang, T.; Chuang, H.-J.; Zhou, Z.; Xu, Y.-Q. Anisotropic Photocurrent Response at Black Phosphorus-MoS_2 P-N Heterojunctions. *Nanoscale* **2015**, *7*, 18537−18541.

(19) Konstantatos, G.; Badioli, M.; Gaudreau, L.; Osmond, J.; Bernechea, M.; De Arquer, F. P. G.; Gatti, F.; Koppens, F. H. Hybrid Graphene-Quantum Dot Phototransistors with Ultrahigh Gain. *Nat. Nanotechnol.* **2012**, *7*, 363−368.

(20) Sun, Z. H.; Liu, Z. K.; Li, J. H.; Tai, G. A.; Lau, S. P.; Yan, F. Infrared Photodetectors Based on CVD-Grown Graphene and PbS Quantum Dots with Ultrahigh Responsivity. *Adv. Mater.* **2012**, *24*, 5878−5883.

(21) Lee, Y.; Kwon, J.; Hwang, E.; Ra, C.-H.; Yoo, W. J.; Ahn, J.-H.; Park, J. H.; Cho, J. H. High-Performance Perovskite-Graphene Hybrid Photodetector. *Adv. Mater.* **2015**, *27*, 41−46.

(22) Xie, C.; You, P.; Liu, Z.; Li, L.; Yan, F. Ultrasensitive Broadband Phototransistors Based on Perovskite/Organic-Semiconductor Vertical Heterojunctions. *Light: Sci. Appl.* **2017**, *6*, E17023.

(23) Kang, D.-H.; Pae, S. R.; Shim, J.; Yoo, G.; Jeon, J.; Leem, J. W.; Yu, J. S.; Lee, S.; Shin, B.; Park, J.-H. An Ultrahigh-Performance Photodetector Based on A Perovskite-Transition-Metal-Dichalcogenide Hybrid Structure. *Adv. Mater.* **2016**, *28*, 7799−7806.

(24) Wang, J.; Yao, Q.; Huang, C.-W.; Zou, X.; Liao, L.; Chen, S.; Fan, Z.; Zhang, K.; Wu, W.; Xiao, X.; Jiang, C.; Wu, W.-W. High Mobility MoS_2 Transistor with Low Schottky Barrier Contact by Using Atomic Thick H-BN as A Tunneling Layer. *Adv. Mater.* **2016**, *28*, 8302−8308.

(25) Ma, C.; Shi, Y.; Hu, W.; Chiu, M.-H.; Liu, Z.; Bera, A.; Li, F.; Wang, H.; Li, L.-J.; Wu, T. Heterostructured WS_2/$CH_3NH_3PbI_3$ Photoconductors with Suppressed Dark Current and Enhanced Photodetectivity. *Adv. Mater.* **2016**, *28*, 3683−3689.

(26) Lu, J.; Carvalho, A.; Liu, H.; Lim, S. X.; Castro Neto, A. H.; Sow, C. H. Hybrid Bilayer WSe_2-$CH_3NH_3PbI_3$ Organolead Halide Perovskite as A High-Performance Photodetector. *Angew. Chem., Int. Ed.* **2016**, *55*, 11945−11949.

(27) Chen, Q.; Zhou, H. P.; Fang, Y. H.; Stieg, A. Z.; Song, T.-B.; Wang, H.-H.; Xu, X. B.; Liu, Y. S.; Lu, S. R.; You, J. B. The Optoelectronic Role of Chlorine in $CH_3NH_3PbI_3$ (Cl)-Based Perovskite Solar Cells. *Nat. Commun.* **2015**, *6*, 7269.

(28) Grancini, G.; Kandada, A. R. S.; Frost, J. M.; Barker, A. J.; De Bastiani, M.; Gandini, M.; Marras, S.; Lanzani, G.; Walsh, A.; Petrozza, A. Role of Microstructure in The Electron-Hole Interaction of Hybrid Lead Halide Perovskites. *Nat. Photonics* **2015**, *9*, 695−701.

(29) Rhoderick, E. H.; Williams, R. H. *Metal-Semiconductor Contacts*, 2nd ed.; Clarendon Press; Oxford University Press: Oxford, 1988; pp 38−40.

(30) Yap, W. C.; Yang, Z.; Mehboudi, M.; Yan, J. A.; Barraza-Lopez, S.; Zhu, W. Layered Material GeSe and Vertical GeSe/MoS_2 P-N Heterojunctions. *Nano Res.* **2018**, *11*, 420−430.

(31) Shah, J. M.; Li, Y. L.; Gessmann, T.; Schubert, E. F. Experimental Analysis and Theoretical Model for Anomalously High Ideality Factors ($N \gg 2.0$) in AlGaN/GaN P-N Junction Diodes. *J. Appl. Phys.* **2003**, *94*, 2627−2630.

(32) Cheng, R.; Li, D.; Zhou, H.; Wang, C.; Yin, A.; Jiang, S.; Liu, Y.; Chen, Y.; Huang, Y.; Duan, X. Electroluminescence and Photocurrent Generation from Atomically Sharp WSe_2/MoS_2 Heterojunction P-N Diodes. *Nano Lett.* **2014**, *14*, 5590−5597.

(33) Li, H.-M.; Lee, D.; Qu, D.; Liu, X.; Ryu, J.; Seabaugh, A.; Yoo, W. J. Ultimate Thin Vertical P-N Junction Composed of Two-Dimensional Layered Molybdenum Disulfide. *Nat. Commun.* **2015**, *6*, 6564.

(34) Baugher, B. W. H.; Churchill, H. O. H.; Yang, Y.; Jarillo-Herrero, P. Optoelectronic Devices Based on Electrically Tunable P-N Diodes in A Monolayer Dichalcogenide. *Nat. Nanotechnol.* **2014**, *9*, 262−267.

(35) Wang, X.; Cheng, Z.; Xu, K.; Tsang, H. K.; Xu, J.-B. High-Responsivity Graphene/Silicon-Heterostructure Waveguide Photodetectors. *Nat. Photonics* **2013**, *7*, 888−891.

(36) Lv, P.; Zhang, X.; Zhang, X.; Deng, W.; Jie, J. High-Sensitivity and Fast-Response Graphene/Crystalline Silicon Schottky Junction-Based Near-IR Photodetectors. *IEEE Electron Device Lett.* **2013**, *34*, 1337−1339.

(37) Shao, D. L.; Gao, J.; Chow, P.; Sun, H. T.; Xin, G. Q.; Sharma, P.; Lian, J.; Koratkar, N. A.; Sawyer, S. Organic−Inorganic Heterointerfaces for Ultrasensitive Detection of Ultraviolet Light. *Nano Lett.* **2015**, *15*, 3787−3792.

(38) Liu, X.; Gu, L. L.; Zhang, Q. P.; Wu, J. Y.; Long, Y. Z.; Fan, Z. Y. All-Printable Band-Edge Modulated ZnO Nanowire Photodetectors with Ultra-High Detectivity. *Nat. Commun.* **2014**, *5*, 4007.

(39) Xie, C.; Mak, C.; Tao, X.; Yan, F. Photodetectors Based on Two-Dimensional Layered Materials Beyond Graphene. *Adv. Funct. Mater.* **2017**, *27*, 1603886.

(40) Gong, X.; Tong, M.; Xia, Y.; Cai, W.; Moon, J. S.; Cao, Y.; Yu, G.; Shieh, C.-L.; Nilsson, B.; Heeger, A. J. High-Detectivity Polymer Photodetectors with Spectral Response from 300 to 1450 nm. *Science* **2009**, *325*, 1665−1667.

(41) Wei, Y.; Ren, Z.; Zhang, A.; Mao, P.; Li, H.; Zhong, X.; Li, W.; Yang, S.; Wang, J. Hybrid Organic/PbS Quantum Dot Bilayer Photodetector with Low Dark Current and High Detectivity. *Adv. Funct. Mater.* **2018**, *28*, 1706690.

(42) Gong, F.; Luo, W.; Wang, J.; Wang, P.; Fang, H.; Zheng, D.; Guo, N.; Wang, J.; Luo, M.; Ho, J. C.; Chen, X.; Lu, W.; Liao, L.; Hu, W. High-Sensitivity Floating-GaTe Phototransistors Based on WS_2 and MoS_2. *Adv. Funct. Mater.* **2016**, *26*, 6084−6090.

(43) Wang, X.; Wang, P.; Wang, J.; Hu, W.; Zhou, X.; Guo, N.; Huang, H.; Sun, S.; Shen, H.; Lin, T.; Tang, M.; Liao, L.; Jiang, A.;

Sun, J.; Meng, X.; Chen, X.; Lu, W.; Chu, J. Ultrasensitive and Broadband MoS$_2$ Photodetector Driven by Ferroelectrics. *Adv. Mater.* **2015**, *27*, 6575−6581.

(44) Liu, S.; Wei, Z.; Cao, Y.; Gan, L.; Wang, Z.; Xu, W.; Guo, X.; Zhu, D. Ultrasensitive Water-Processed Monolayer Photodetectors. *Chem. Sci.* **2011**, *2*, 796−802.

(45) Li, C.; Cao, Q.; Wang, F.; Xiao, Y.; Li, Y.; Delaunay, J.-J.; Zhu, H. Engineering Graphene and TMDS Based Van Der Waals Heterostructures for Photovoltaic and Photoelectrochemical Solar Energy Conversion. *Chem. Soc. Rev.* **2018**, *47*, 4981−5037.

(46) Feng, W.; Jin, Z.; Yuan, J.; Zhang, J.; Lou, J.; et al. A Fast and Zero-Biased Photodetector Based on GaTe-InSe Vertical 2D P-N Heterojunction. *2D Mater.* **2018**, *5*, 025008.